

Mar.2018 / Vol.161

M i t s u b i s h i E l e c t r i c

# ADVANCE

Optical & High-Frequency Devices

• **Editorial-Chief**

*Tomoyuki Kobayashi*

• **Editorial Advisors**

*Toshio Masujima  
Naoshi Sakai  
Masayuki Sato  
Hiroaki Sakai  
Akihide Shiratsuki  
Chikao Nishida  
Hitoshi Suzuki  
Kunihiko Egawa  
Shinichi Kuroda  
Masanori Torii  
Hiroaki Imamura  
Hideyuki Takasago  
Noboru Shirakura  
Takayuki Hayashi  
Toshihiro Kurita*

• **Vol. 161 Feature Articles Editor**

*Toshitaka Aoyagi*

• **Editorial Inquiries**

*Tomoyuki Kobayashi*  
Corporate Total Productivity Management  
& Environmental Programs  
Fax: +81-3-3218-2465

• **Product Inquiries**

**NORTH AMERICA**

Mitsubishi Electric US, INC  
Semiconductor Division  
5900-A Katella Avenue, PO BOX 6007,  
Cypress, CA 90630-5019, U.S.A.  
*Danyo Tu*  
E-mail: Mitsubishi.HFOpto@meus.mea.com

**GERMANY**

Mitsubishi Electric Europe B.V.  
German Branch  
Semiconductor - European Business Group  
Mitsubishi-Electric-Platz 1, 40882 Ratingen,  
Germany  
*Corinna Meyer*  
Fax: +49-(0)2102-486 4140

**CHINA**

Mitsubishi Electric & Electronics (Shanghai)  
Co., Ltd  
29 Floor, Shanghai MAXDO Center No. 8,  
Xing Yi Road, Hong Qiao, Shanghai  
200336, China  
*Qian Yu Feng*  
Fax: +86-21-5208-1502

**Mitsubishi Electric Advance** is published on line quarterly (in March, June, September, and December) by Mitsubishi Electric Corporation. Copyright © 2018 by Mitsubishi Electric Corporation; all rights reserved. Printed in Japan.

The company names and product names described herein are the trademarks or registered trademarks of the respective companies.

**CONTENTS**

**Technical Reports**

Overview ..... 1  
by *Hitoshi Watanabe*

Direct Modulation DFB Laser  
for 25 Gbps Optical Transmission ..... 2  
by *Go Sakaino and Mizuki Shirao*

100 Gbps Compact Integrated EML-TOSA ..... 5  
by *Yudai Imai and Tatsuo Hatta*

Compact Integrated APD ROSA for QSFP28 ..... 8  
by *Tadayoshi Hata and Nobuo Ohata*

Red Laser Diode with 2.1-W CW Operation for Projectors ..... 11  
by *Kyosuke Kuramoto and Shinji Abe*

High Gain and High Power Ku-band GaN HEMT for Satellite  
Communication ..... 14  
by *Tetsuo Kunii and Hiroaki Maehara*

Analysis of Radiation Resistance in GaN HEMT ..... 17  
by *Takayuki Hisaka, Hajime Sasaki, Shinobu Onoda and Takeshi Ohshima*

**Precis**

In the advanced information society, higher-speed, higher-power, and more reliable optical and microwave devices are in demand. This article introduces new optical and microwave devices as well as their related analysis techniques, which have been developed by Mitsubishi Electric Corporation for use in optical fiber links, projectors, and satellite communications.

# Overview



Author: *Hitoshi Watanabe\**

## Status and Outlook of Optical & High-Frequency Devices

With the global spread of smartphones and other information devices, we now live in an environment where not only data communication but also images and sounds are available any time, anywhere, causing an exponential increase in the amount of data handled. The communications infrastructure relies on high-frequency devices and optical devices using compound-semiconductor that can handle large amount of data. In the field of mobile communication, discussions on communications standards for the 5th generation (5G) following the 4th generation (4G) have already started. This standardization will require high-frequency devices using GaN (gallium nitride) which enable efficient operation at high-frequencies (3.5 GHz to millimeter wavebands) due to the wide communication bandwidth and downsized equipments. And optical devices, that can operate at high speed (25 Gbps to 400 Gbps) yet low power consumption, will be also required.

Meanwhile, in the field of access networks, which are at the end of an optical communication network, 40 Gbps-class next-generation passive optical network systems are being developed. In the field of data centers, which are making remarkable progress, 400 Gbps standards are going to be established. Accordingly, in both fields, optical communication devices that can operate at high speed with low power consumption will also become the key components. In other fields, GaAs (gallium arsenide) semiconductor laser for projector light sources, laser processing machines, etc. is steadily being developed. Thus, the demand for high-frequency devices and optical devices using compound semiconductors is growing, and such devices will become increasingly critical in various scenes in the society.

# Direct Modulation DFB Laser for 25 Gbps Optical Transmission

Authors: Go Sakaino\* and Mizuki Shirao\*\*

## 1. Introduction

For the next-generation system defined by the Common Public Radio Interface (CPRI) standard for mobile communication systems, it is necessary to develop a high-speed transceiver (25 Gbps) for communication devices. In addition, operation at high temperatures is required for antenna base station communication devices installed outdoors. To meet these needs, we have developed a 25 Gbps distributed feedback (DFB) laser that operates over a wide temperature range ( $-20^{\circ}\text{C}$  to  $85^{\circ}\text{C}$ ) at high speed.

## 2. Device Design

In the past, we developed laser chips that operate at 25 Gbps within the temperature range of  $-5^{\circ}\text{C}$  to  $75^{\circ}\text{C}$  as uncooled direct modulation DFB lasers. To extend this range, it is necessary to minimize the decrease in optical output and the increase in operating current at high temperatures. To this end, it is important to suppress the deterioration of optical modulation waveforms caused by light oscillation resulting from the laser-inherent interaction between electricity and light. The frequency of this light oscillation is called the relaxation oscillation frequency ( $f_r$ ). To obtain a desirable optical modulation waveform, it is necessary to maintain  $f_r$  at a high value at a high modulation signal frequency level. This can be achieved by suppressing the phenomena that are remarkable due to a high temperature, i.e., increased optical loss, reduced efficiency of current injection into the active region, and reduced optical density in the active region entailing a drop in  $f_r$ . Based on a laser chip structure that operates at 25 Gbps within a temperature range of  $-5^{\circ}\text{C}$  to  $75^{\circ}\text{C}$ , we redesigned the structure around the active region. As a result, we achieved a balanced structure between high-temperature, low-loss effective current injection into the active region even at  $85^{\circ}\text{C}$ , and stable high slope efficiency.

The package with the DFB laser also needs an increase in speed from 10 Gbps to 25 Gbps, i.e., 2.5 times. This involves two challenges: One relates to the modulation bandwidth of TO-CAN packages. Leads and inner gold wires for transmitting electrical signals inside a TO-CAN package can degrade the high-frequency properties of the entire package. By eliminating the inductance inside a TO-CAN package for 10 Gbps operation, the internal impedance was optimized. As shown in Fig. 1, the optical waveform

quality was significantly improved for 25 Gbps operation, which has been difficult to achieve with a 10 Gbps TO-CAN package.

The other challenge involves deterioration of the waveform quality due to the multiple reflection of electricity. While a normal DFB laser has resistance of approx.  $12\ \Omega$ , signal lines are designed using differential lines with characteristic impedance of  $50\ \Omega$ . In this configuration, the inconsistent impedance is likely to make the reflection of high-frequency signals larger, involving waveform quality that is susceptible to deterioration due to multiple reflection to each connection point. The junction to a flexible printed circuit (FPC) as an electrical interface of a TO-CAN package in particular tends to be a multiple reflection point. Figure 2 shows the configuration at the junction between the stem, which is the main body of a TO-CAN package, and the FPC. In conventional 10 Gbps TO-CAN packages, an insulation sheet of approx. 0.1 mm thick is inserted between the FPC ground plane and the stem. With the interspace represented by G (gap), the simulation results for the small signal response properties of the TO-CAN

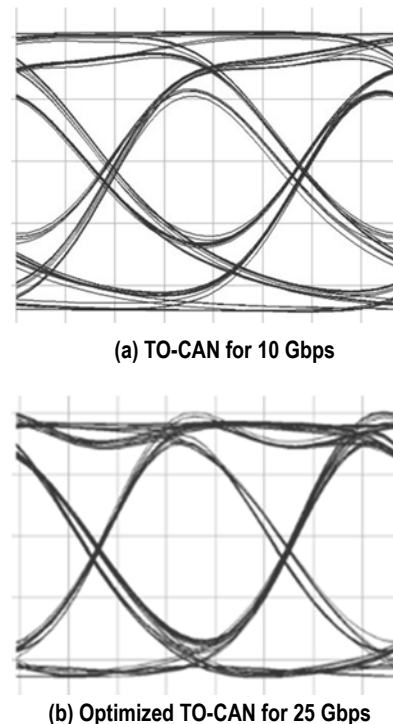


Fig. 1 Simulated waveforms of TO-CAN with the 25 Gbps DFB laser

package with the 25 Gbps DFB laser are shown in Fig. 3; the simulation results for the optical waveforms are shown in Fig. 4. During the 25 Gbps operation, the properties to allow signal passage and the optical waveform quality were confirmed to have deteriorated even when the gap was small. Given the fact that the small discontinuous impedance and the inductance component increase due to the gap, causing property deterioration, configuration (a) without a gap was adopted for the prototype.

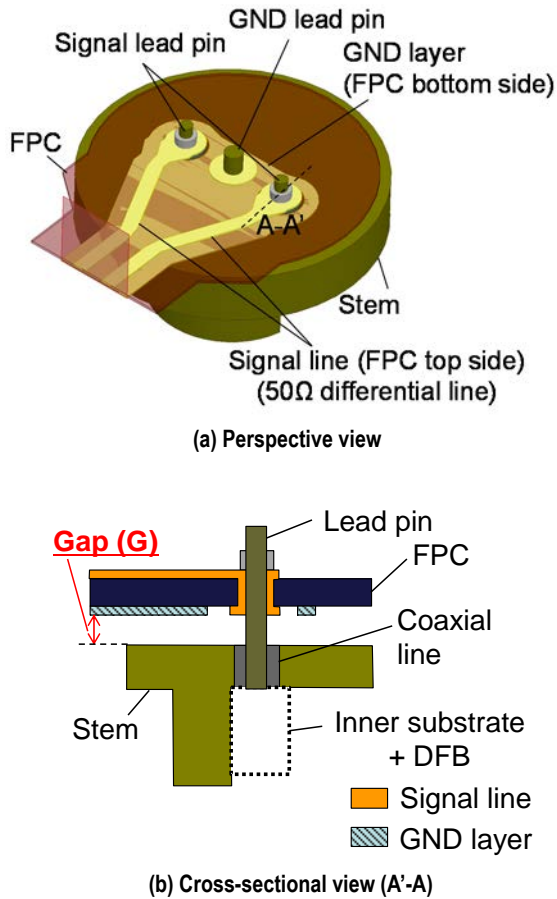


Fig. 2 Simulation model of TO-CAN

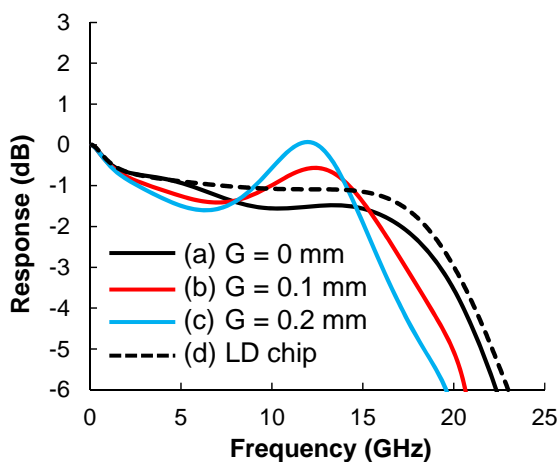


Fig. 3 Simulated frequency response of the 25 Gbps DFB laser

### 3. Device Structure and Characteristics

We produced a 25 Gbps DFB laser with the structure shown in Fig. 5, based on the design as described above. The DFB laser chip was mounted on the newly designed  $\Phi 5.6$  mm TO-CAN package described above. Via the internal substrate built into the TO-CAN package, the DFB laser chip was connected to external leads. A cap with a lens to link the emitted light to optical fiber, and to hermetically seal a laser chip was also mounted.

Figure 6 shows the current vs. optical output properties of the DFB laser. The threshold current and slope efficiency did not excessively depend on the temperature, and thus good characteristics were obtained. At a high temperature, e.g. 85°C, the threshold current did not exceed 16 mA, and the slope efficiency did not drop lower than 0.17 mW/mA. A maximum optical output of at least 10 mW was obtained.

We evaluated 25.8 Gbps optical modulation waveforms in the temperature range of  $-20^{\circ}\text{C}$  to  $85^{\circ}\text{C}$ . Through the FPC, pseudo-random NRZ signals (non-return-to-zero signal) of 25.78 Gbps were input from a PPG (pulse pattern generator). The obtained modulation waveforms are shown in Fig. 7. Clear shapes were obtained within the temperature range between  $-20^{\circ}\text{C}$  and  $85^{\circ}\text{C}$ . When the CWDM4 mask was used, the mask margin (MM), which indicates the modulation waveform quality, had desirable values of 40%, 40% and 39% at  $-20^{\circ}\text{C}$ ,  $25^{\circ}\text{C}$  and  $85^{\circ}\text{C}$ , respectively. With the 100GBASE-LR4 mask, which requires higher waveform quality than CWDM4, the mask margin was high at 23%, 28% and 25% for each temperature. From these results, we confirmed that the DFB laser properties were sufficient for 25 Gbps optical transmission; the use of the DFB laser allowed us to perform low-current operation with the average current not exceeding 61 mA, and to obtain desirable mask margin values even at a high temperature of  $85^{\circ}\text{C}$ . We believe that these properties will be useful for mobile communication systems

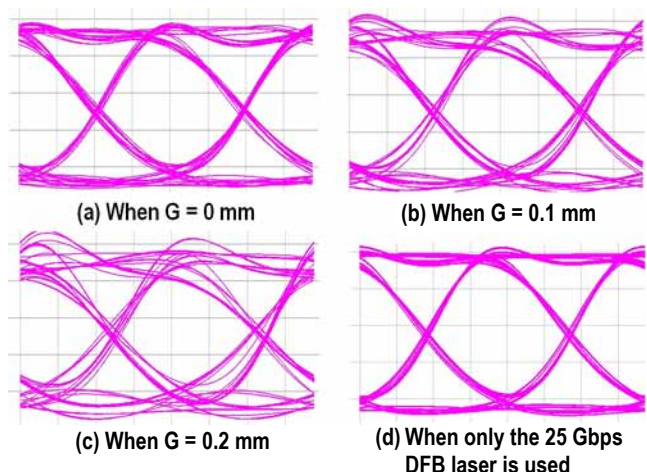


Fig. 4 Simulated waveforms with 25Gbps modulation



Fig. 5 25 Gbps DFB laser

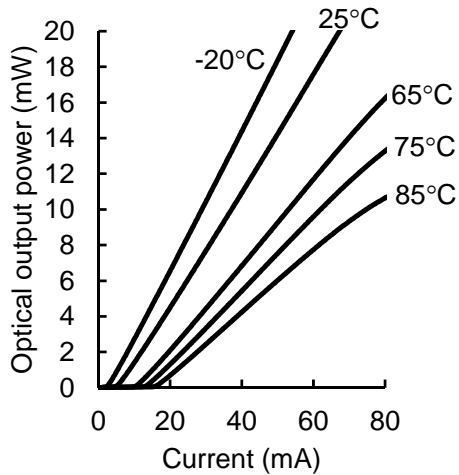
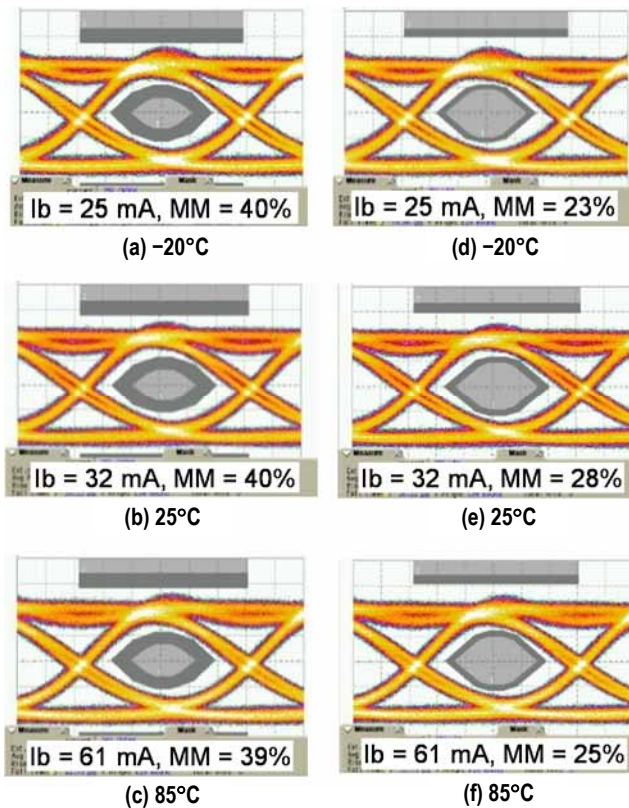


Fig. 6 I-L characteristics (-20, 25, 65, 75, 85°C)

conforming to the 25 Gbps operation small transceiver standard (SFP28), and can play a significant role in increasing the speed and reducing the power consumption of mobile communication systems.

#### 4. Conclusion

The developed product described here will contribute to the conformity of mobile communication systems to the 25 Gbps operation small transceiver standard (SFP28), as well as help increase the speed and reduce the power consumption of mobile communication systems by means of uncooled operation.



Ib: Average current  
MM: Mask margin ((a) to (c): CWDM4, (d) to (f): LR4)

Fig. 7 25.78 Gbps waveforms  
(Optical output power: 8 mW; Extinction ratio: 5 dB)

# 100 Gbps Compact Integrated EML-TOSA

Authors: *Yudai Imai\** and *Tatsuo Hatta\**

## 1. Introduction

Along with the increase in speed and capacity of optical transmission devices, the use of 100 Gbps optical networks is rapidly expanding. To cope with the increase in traffic, 100 Gbps optical transceivers need to be downsized and able to operate with less power. We have developed a compactly integrated 100 Gbps electroabsorption modulator laser (EML) diode transmitter optical subassembly (TOSA) that is small in size and capable of low power consumption operation. This has been achieved by using four lenses precisely fixed in a close-packed manner for the respective four EMLs, and by embedding the laser in each EML to increase the efficiency.

## 2. Device Specifications

The compactly integrated 100 Gbps EML-TOSA that we developed complies with 100GBASE-LR4 specifications defining transmission at a distance of 10 km standardized by IEEE, 100GBASE-ER4 specifications defining transmission at a distance of 40 km, and application code 411-9D1F recommended by the ITU-T. The EML-TOSA operates within a case temperature range of  $-5^{\circ}\text{C}$  to  $80^{\circ}\text{C}$ , up to a maximum bit rate of 27.95 Gbps.

## 3. Device Design

Figure 1 is a photo of the device. For the package, metal and ceramic are used in an integrated manner. For the electrical signal interface, two flexible printed circuits (FPCs) for radio frequency (RF) connection to allow modulating signals to pass through and for DC connection to supply power to the laser diode (LD), photodiode (PD), and thermoelectric cooler (TEC) are provided for connection to the package. The FPCs are directly connected to the metal pattern, the pitch of which has been narrowed on the ceramic to make the package compact. The FPC for RF connection has a three-layered

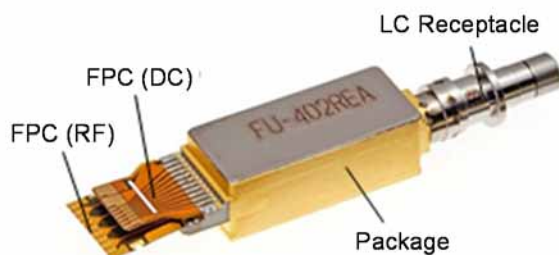


Fig. 1 100 Gbps compact integrated EML-TOSA

structure; ideal impedance matching has been achieved by placing signal wires at an FPC inner layer to be free from constraints related to the electrode interval required to prevent short circuits at the connection. The size of the package is  $15.0 \times 6.5 \times 5.4$  mm, which is approximately two-thirds the volume of our conventional products.

## 4. EML Design

Figure 2 shows schematic views of the EML device structure. The laser is embedded to ensure excellent efficiency and operation at high temperatures. The electroabsorption (EA) modulator is extended in length and reduced in width to achieve a balance between low modulation voltage and high-speed operation. The EA modulator is a high mesa type, which can keep the optical confinement coefficient high regardless of the narrowed width.<sup>(1)</sup> As described above, the laser and EA modulator are provided with separate waveguide structures, allowing them to individually exert excellent properties.

## 5. Optical System and Mechanism Design

Figure 3 shows a conceptual diagram of the optical system in the TOSA. In the package, four EMLs, four lenses, and a special optical system multiplexer are integrated. The optical multiplexer consists of three bandpass filters (BPFs) and a mirror, and is fixed to a block member. The product uses a double-lens optical system. The first lens is mounted inside the package, and the second lens is arranged outside the package. Collimated light passing through the first lens enters the special optical system multiplexer. The light is multiply reflected between the BPFs and mirror, thereby multiplexing four wavelengths of lanes 0, 1, 2 and 3.<sup>(2)</sup> Furthermore, as it is essential for downsizing the package to mount the four lenses in the package in a close-packed and highly precise manner, we have developed a technology to align and fix lenses to submicron order; this has allowed the lens spacing to be reduced to approximately two-thirds that of conventional products.

## 6. Evaluation Results

Figure 4 shows optical waveforms at a modulation speed of 27.95 Gbps. The EMLs modulated all lanes at the same time. The test pattern used was an optical waveform of NRZ PRBS 231-1 before transmission after passing through a fourth Bessel-Thomson filter. Under the condition of EA modulator voltage magnitude of

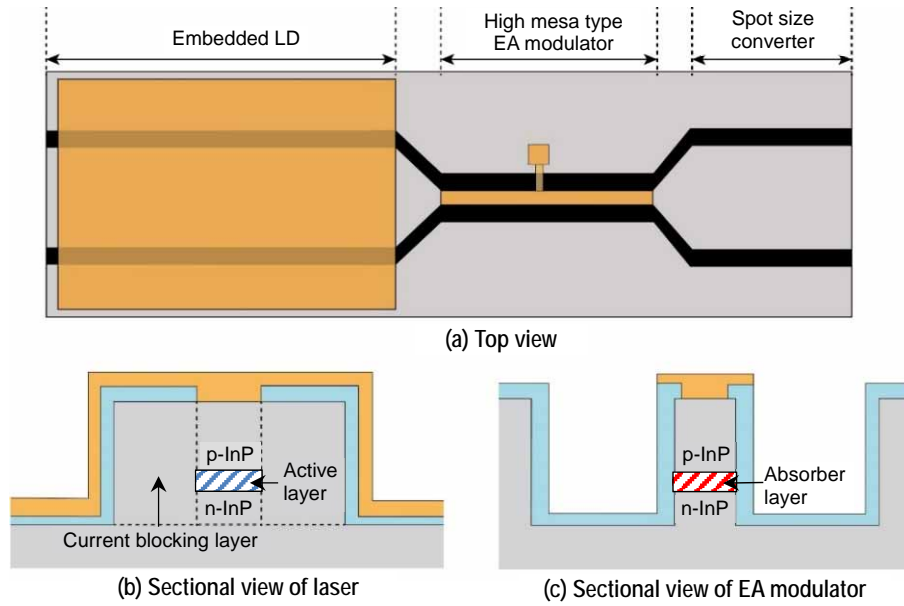


Fig. 2 Structure of EML

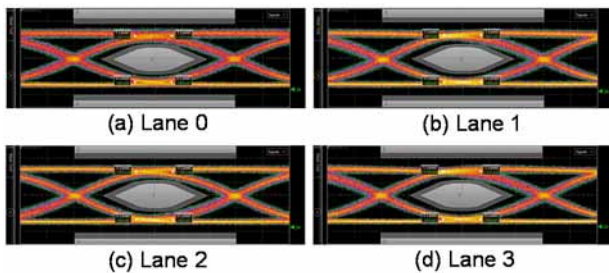
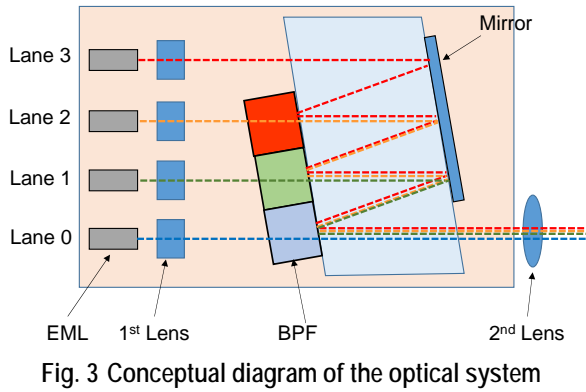


Fig. 4 Optical waveform

1.75 V for all lanes, we obtained results consisting of an extinction ratio not less than 9 dB, and desirable eye-opening characteristics with the mask margin not less than 20% for the eye mask specified by the ITU-T. The average optical output for each lane was 0.36 to 0.43 dBm, indicating that the obtained optical output had less variation between lanes. The case temperature variation (tracking error properties) of the average optical output did not exceed 0.5 dB for any of the lanes at any temperatures in the operating temperature range (-5°C to 80°C), showing that the optical output properties were very stable.

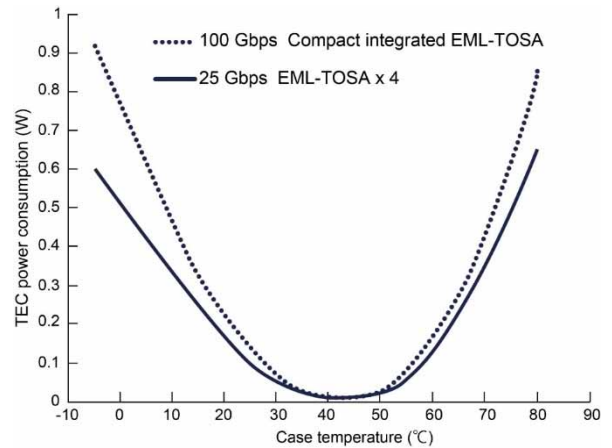


Fig. 5 TEC power consumption

Figure 5 shows the power consumption of the TEC. The operating temperature of the EMLs is set between 50°C and 60°C to be adjusted to the wavelength of the LAN-WDM standard. If the operating temperature of EMLs is set low, the temperature difference increases when the environment temperature is high, causing the TEC power consumption to increase. By setting the operating temperature of EMLs to 50°C or more, the product can keep the TEC power consumption at 0.8 W or less within the operating temperature range of -5°C to 80°C, at a level that allows its use in a small transceiver (QSFP + platform). For comparison, Fig. 5 also shows the power consumption when using four 25 Gbps TOSAs manufactured by Mitsubishi Electric Corporation. With the compactly integrated 100 Gbps EML-TOSA, power consumption was reduced by approximately 0.2 W when the case temperature was 80°C, and by approximately 0.3 W when the case temperature was -5°C.

## 7. Conclusion

We have commercialized a new 100 Gbps EML-TOSA that is compactly integrated to downsize the package and that operates with less power than conventional products. We will continuously strive to satisfy the ever-growing need for higher-speed operation, lower power consumption and smaller size of optical transmission devices, using and reinforcing the developed product technology.

## References

- (1) Yamatoya, T., et al.: Low-Voltage and High-Temperature Operation of 28 Gb/s EMLs with Hybrid Waveguide Structure for Next-Generation 100GbE Transceivers, IEICE GENERAL Conference C-4-18 (2013)
- (2) Tadashi, M., et al.: Integrated Spatial Optical System for Compact 100GbE Transmitter Optical Sub-Assemblies Using Lens Positional Control by Laser Irradiation, Proceedings of the IEICE(LQE) (2015)

# Compact Integrated APD ROSA for QSFP28

Authors: Tadayoshi Hata\* and Nobuo Ohata\*

## 1. Background

The continuous increase in communication traffic requires faster, higher-capacity optical communication devices. The demand for high-speed optical transceivers that operate at 100 Gbit/s is growing. Currently, the industry-standard CFP transceivers<sup>(1)</sup> constitute the majority of the optical transceiver market; at the same time, development is underway on the QSFP28 (quad small form factor pluggable), which will be approximately one-fourteenth the volume ratio. CFP transceivers supporting transmission distance of the 40-km has a significant transmission loss due to long distance optical fiber transmission. Therefore, it is necessary to use a semiconductor optical amplifier (SOA) in front of a photodiode (PD) receiver optical subassembly (ROSA), hindering downsizing. Against this backdrop, a study was started on 40-km transmission using an avalanche photodiode (APD) ROSA alone, and was standardized by ITU-T for 4L1-9D1F in G.959.1.<sup>(2)</sup> Table 1 shows the specifications. This article describes the development of an APD ROSA that complies with the standard and is capable of being applied to a QSFP28 by speeding up the APD.

Table 1 Target specifications of the APD ROSA

Bit rates		27.95249 Gbit/s
Wavelength	Lane 0	1294.53 – 1296.59 nm
	Lane 1	1299.02 – 1301.09 nm
	Lane 2	1303.54 – 1305.63 nm
	Lane 3	1308.09 – 1310.19 nm
Minimum receiver sensitivity		-18.9 dBm

## 2. Configuration of the APD ROSA

Figure 1 shows a schematic view of the APD ROSA configuration. Received signals are optical signals multiplexed using four different wavelengths. An optical signal is converted to collimated light using a collimating lens, and is separated into four signals with different wavelengths by a demultiplexer. The separated optical signals are concentrated into the APD of each Lane by four lenses. In the APD, the optical signal is amplified and converted to an electric current, which is then converted to a voltage signal by a transimpedance amplifier (TIA) to be output from a ROSA.

## 3. Designing the APD

To achieve high receiver sensitivity, a wide bandwidth, high responsivity, and low dark currents necessary for operation at 28 Gbit/s even when using an APD alone are required. Figure 2 shows a schematic view of the APD configuration using a planar backside illumination structure. In the planar structure, a p-n junction is partially formed in the epilayer. As the structure can easily prevent the degraded p-n interface from being exposed to the outside, so that the dark currents can be reduced. Furthermore, the backside illumination structure light to enter from the back of the substrate to an absorption layer that formed on the substrate surface using epitaxy. Light that has passed through the absorption layer is reflected by the mirror on the outermost surface and then is absorbed again in the absorption layer, thus increasing the sensitivity.

When designing the device considering the receiver sensitivity and bandwidth, the thicknesses of the

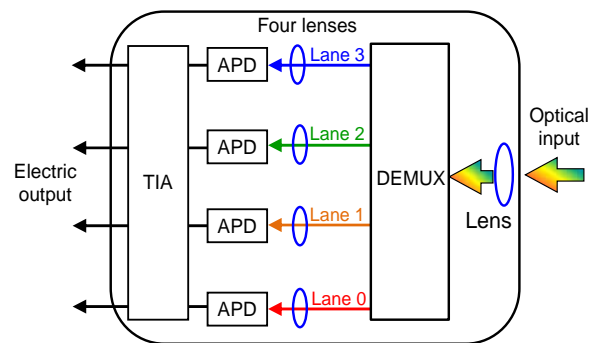


Fig. 1 Components of the APD ROSA

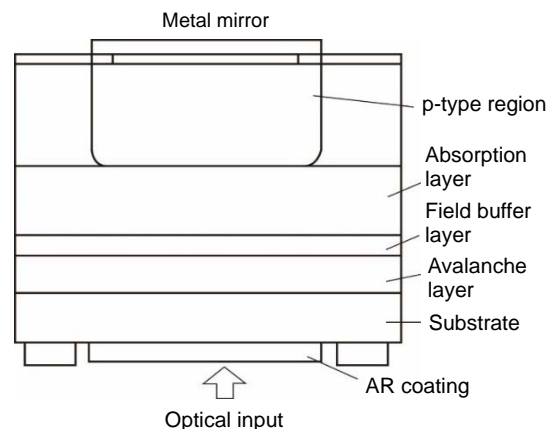


Fig. 2 Structure of the APD

avalanche layer and absorption layer are important. The drift velocity of holes is slow compared with that of electrons, and thus the multiplication of holes deteriorate the bandwidth. When the avalanche layer is made thinner, the multiplication of holes can be suppressed, thereby improving the bandwidth. This means that a thin avalanche layer is desirable for broadening the bandwidth. However, the thin avalanche layer has the disadvantage that the dark currents increases. For the avalanche layer of the APD, a thickness that can balance the properties between the bandwidth and dark currents has been chosen. Figure 3 shows the calculation results of the absorption layer thickness and the 3-dB frequency bandwidth at a multiplication factor of 10. The absorption layer thickness was determined to be 600 nm, which maximizes the bandwidth, to 18.5 GHz. With this thickness, a favorable responsivity at approximately 0.8 A/W can be achieved.

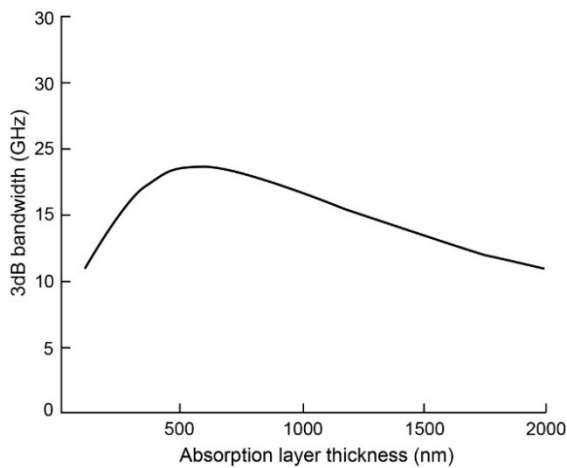


Fig. 3 3-dB down bandwidth versus absorption layer thickness

#### 4. Design of the APD ROSA

To achieve the desired minimum receiver sensitivity, it is important to reduce the optical loss of the ROSA and to secure the optical isolation of adjacent lanes, which are both largely dependent on the demultiplexer. The optical loss should be as small as possible. Therefore, the target value was set to 1.0 dB or less. It is necessary to reduce the optical isolation to a level at which the receiver sensitivity does not deteriorate due to the effects from an adjacent lane. Figure 4 shows a graph of the penalty calculation results for optical isolation. If the optical isolation is 27 dB, the penalty is 0.05 dB or less. Based on these considerations, we used an optical filter with an optical loss of 1.0 dB and optical isolation of 27 dB. The demultiplexer has a structure in which four optical filters were attached to a glass prism.

Figure 5 shows a graph of the calculation results of the demultiplexer spectrum properties. The shaded areas represent the regions with the optical loss at

1.0 dB and optical isolation at 27 dB in the wavelength bandwidth of each lane. For each lane, the filter loss did not exceed 0.6 dB, and the optical isolation from adjacent lanes was at least 30 dB, satisfying the target.

#### 5. Properties of the APD and APD ROSA

Figure 6 shows a graph of the frequency response properties of the APD. With 10 as the multiplication factor, 18 GHz, which is close to the calculated value, was

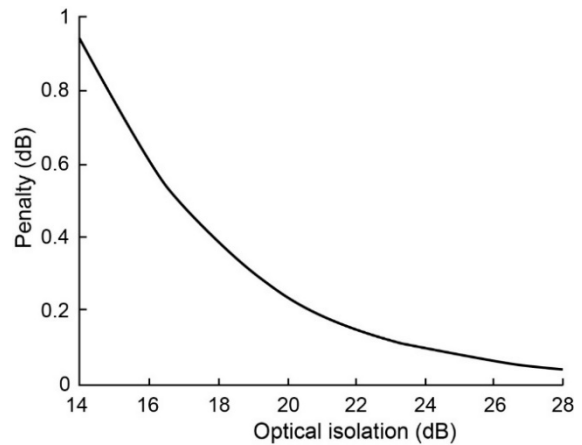


Fig. 4 Penalty versus optical isolation

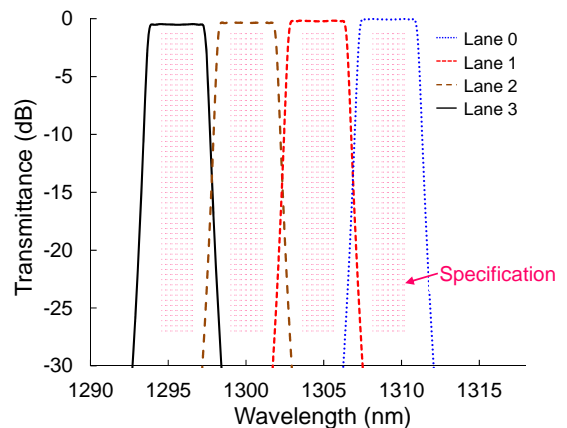


Fig. 5 Spectrum characteristics of the demultiplexer

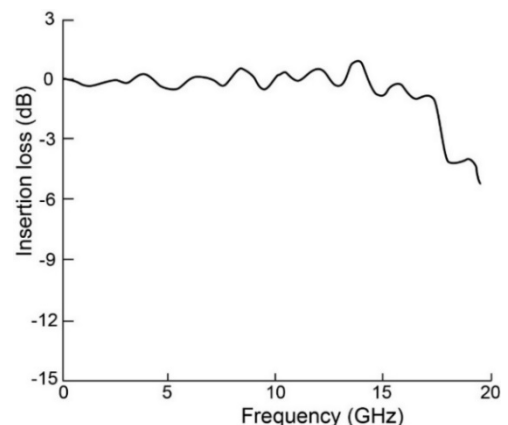


Fig. 6 Insertion loss versus frequency

achieved in the 3-dB bandwidth.<sup>(3)</sup>

Figure 7 shows a graph of the evaluation results of the demultiplexer transmission spectrum. The loss at the demultiplexer did not exceed 0.5 dB, and the optical isolation was at least 30 dB, showing that the designed properties were obtained.

Figure 8 shows a photo of the APD ROSA. The external dimensions are 24.6×6.55×5.1 mm, allowing the device to be mounted on a QSFP28.

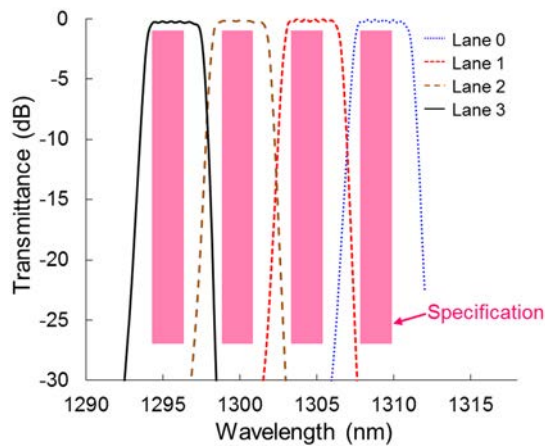


Fig. 7 Spectrum characteristics of the demultiplexer

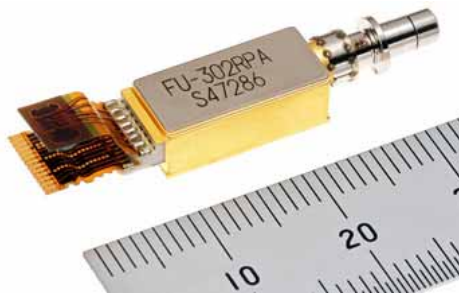


Fig. 8 Photograph of the APD ROSA

Figure 9 shows a graph of the bit error ratio (BER) when the ROSA temperature was 25°C. The light source was modulated at a rate of 27.95249 Gbit/s and with the PRBS2<sup>31</sup>-1 pattern. The optical signal extinction ratio for Lanes 0 to 3 is 8.9, 10, 9.2 and 9.6 dB, respectively. The APD voltage was set to 19 V for all lanes. The minimum receiver sensitivity at an error ratio of 10<sup>-6</sup>, making an allowance for error correction, was -23.7, -24.6, -24.5 and -24.4 dBm for Lanes 0 to 3, respectively. This satisfied the standard specification.

Figure 10 shows the minimum receiver sensitivity when the ROSA temperature was changed from -5°C to 80°C. While the receiver sensitivity dropped to the lowest at 80°C, Lanes 0 to 3 were -22.8, -23.6, -23.8 and -23.7 dBm, respectively, showing that favorable results satisfying the standard specification were obtained. The maximum power consumption was 0.42 W, which is low enough for the device to be applied to a QSFP28.

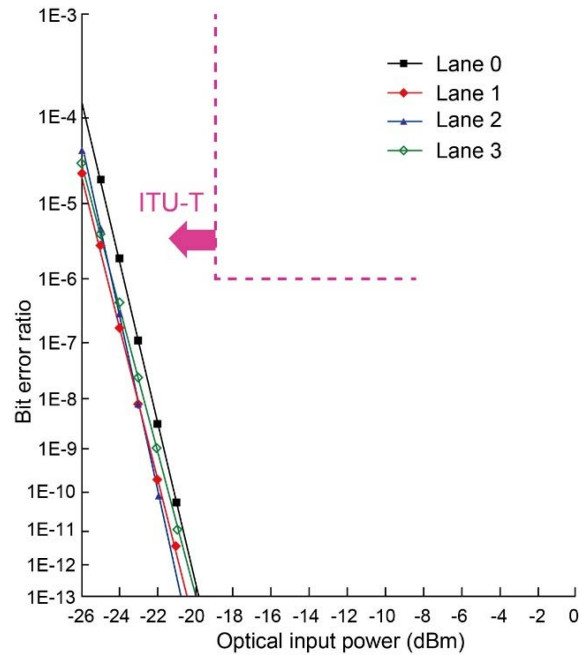


Fig. 9 Bit error ratio

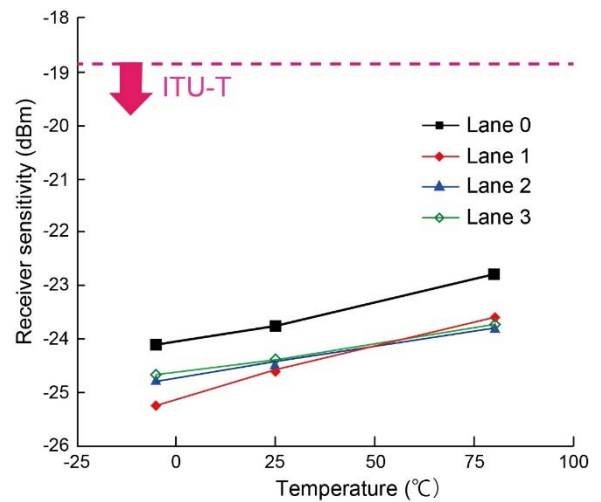


Fig. 10 Minimum receiver sensitivity versus temperature

## 6. Conclusion

We have developed a 100 Gbit/s integrated APD ROSA for 40-km transmission. With downsized external dimensions of 24.6×6.55×5.1 mm and very low maximum power consumption of 0.42 W, the device is suitable for applying to a QSFP28. The minimum receiver sensitivity of achieved -22.8 dBm when the ROSA temperature was changed from -5°C to 80°C, satisfy the ITU-T standard specification.

## References

- (1) CFP-MSA: <http://www.cfp-msa.org>
- (2) ITU-T G.959.1: <http://www.itu.int/en/ITU-T>
- (3) Takemura, R., et al.: "Resonant Cavity 25Gbps APD for high responsivity and low dark current," IEICE General Conference C-4-2 (2016)

# Red Laser Diode with 2.1-W CW Operation for Projectors

Authors: *Kyosuke Kuramoto\** and *Shinji Abe\**

In the pursuit of improved brightness, efficiency, and lifetime of projectors, it is desirable to use semiconductor lasers, i.e. laser diodes (LDs), for the light source. Following a conventional 2.5-W pulse-operated red LD, Mitsubishi Electric Corporation started mass production of a red LD that supports continuous wave (CW) operation at the world's highest<sup>1</sup> 2.1-W output by improving the device structure.

## 1. Introduction

Currently, high-pressure mercury lamps are widely used as the light source for projectors. Such lamps have several disadvantages including a relatively short lifetime of about 3,000 to 6,000 hours, large power consumption, and the environmental load of mercury. Accordingly, mercury lamps used as light sources are being replaced with LDs, which have such advantages as higher efficiency, higher color reproducibility, longer life, and lower environmental load. In September 2015, we started mass production of a red LD light source (ML562G84) capable of 2.5-W pulse operation. Since then, the red LD has gradually penetrated the market as a substitute for mercury lamps.

Projectors can be classified into two types: one that uses a single digital mirror device, and one that uses three digital mirror devices. Pulse light sources are used for the former, while CW light sources are used for the latter. We have developed and placed on the market a

new red semiconductor LD that supports CW operation and 2.1-W output. This article describes the design, device characteristics, and lifetime test results of the high-output red LD.

## 2. Device Structure and Device Design

Figure 1 shows a schematic view of the basic structure of the red LD placed on the market. Using AlGaInP-based material, a broad stripe (BS) LD structure is adopted, which makes it relatively easy to increase the output.

The main reason for the reduced optical output of a red LD at high temperatures is that electrons with thermal energy pass through the band barrier in the p-cladding layer and no longer contribute to the light emission (electron overflow). To prevent this, the new product has a highly doped p-cladding layer. Furthermore, an increase in the amount of light confined in the active layer can suppress the electron overflow by reducing the carrier density required for oscillation.

As a measure for the catastrophic optical damage (COD) deterioration caused by optical absorption in the vicinity of the edges, the emission edge is provided with a window-mirror structure that involves disordering the quantum well structure through our own technique of Zn diffusion. In addition, the front edge is given a low-reflection coating, while the rear edge is given a high-reflection coating.

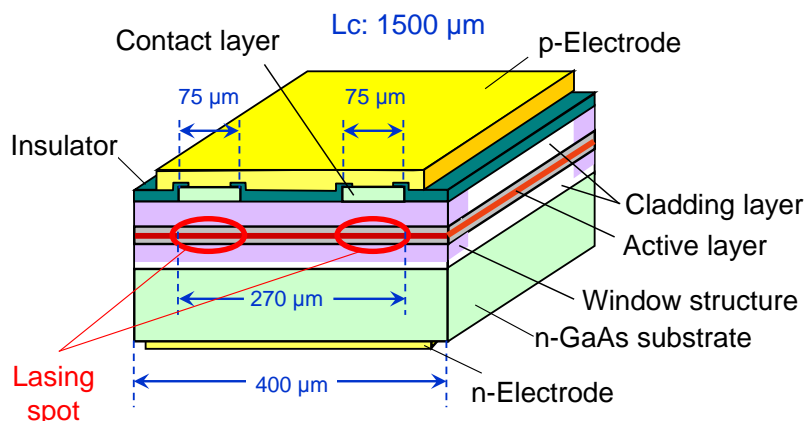


Fig. 1 Device structure of the red LD

<sup>1</sup> As of October 16, 2017 (our own research)

Furthermore, by dividing the light-emitting region into two parts that are 75  $\mu\text{m}$  in width, the heat generation density has been reduced, thereby suppressing the increase in temperature of the active layer. The length of the LD resonator has been determined to be 1,500  $\mu\text{m}$ .

To facilitate efficient heat radiation from the active layer, the device has been assembled using a junction-down method, which involves die bonding the active layer side to the submount, which is then mounted on a TO-CAN package (Fig. 2) which is 9.0 mm in diameter.

The barrier to a power output increase for red LDs is mainly the COD at the front edge. This is a phenomenon in which the edge melts due to optical absorption in the vicinity, resulting in device failure. The average lifetime in such a failure mode, called the mean time to failure (MTTF), tends to be shorter as the optical density at the front edge becomes larger. For this reason, an extremely effective method for ensuring high reliability is to increase the full width of the light-emitting region to reduce the light density.

However, the light-emitting region is also a heat-generating region; an increase in the full stripe width causes the heating value to increase, resulting in reduced optical output at a high temperature or at high output power. Given this, we have selected for the new product a structure with two light-emitting points that are 75  $\mu\text{m}$  in width, as such a structure can achieve a balance between an MTTF of at least 20,000 hours and favorable high temperature properties.

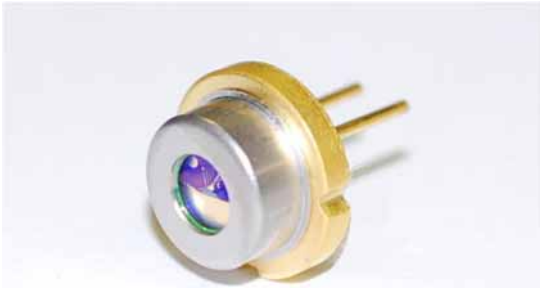


Fig. 2 Appearance of the  $\phi 9.0$  mm TO-CAN

### 3. Device Characteristics and Reliability Evaluation Results

Figure 3 shows a typical graph of the relationship between the optical output and current characteristics of the new red LD. The red LD was operated in CW mode at the temperatures shown in the figure which are the case temperature measured at the package bottom. The operating current of the product at 25°C and 45°C for the output power of 2.1 W was 2.25 A and 2.95 A, respectively; and the operating voltage was 2.27 V and 2.34 V, respectively. The slope efficiency at 25°C was 1.20 W/A.

Figure 4 shows a graph of the far-field pattern (FFP) in the horizontal direction (FFP//) and vertical direction

(FFP $\perp$ ) when the product was CW-operated at 25°C for 2.1-W power output. When the optical output was 1/e<sup>2</sup> of the peak value, the full width in FFP// and FFP $\perp$  was 8.9° and 62.1°, respectively. When the product was CW-operated at 25°C for 2.5-W power output, the wavelength spectrum had a peak waveform of 638.5 nm and a full width at half maximum of approx. 0.9 nm.

When the product was operated at 3.55-W power output in CW mode at the case temperature of 20°C with constant current, the MTTF was 3,990 hours. All deteriorated parts detected were those involving COD. The results from another verification test revealed that the deterioration acceleration involving COD during the 3.55-W operation was 5.90 times that during the 2.1-W power output operation. Therefore, the MTTF during 2.1-W CW operation was equivalent to  $3,990 \times 5.9 = 23,500$  hours.

Figure 5 shows a graph of the lifetime test results by performing CW operation of the product for 2.1-W power

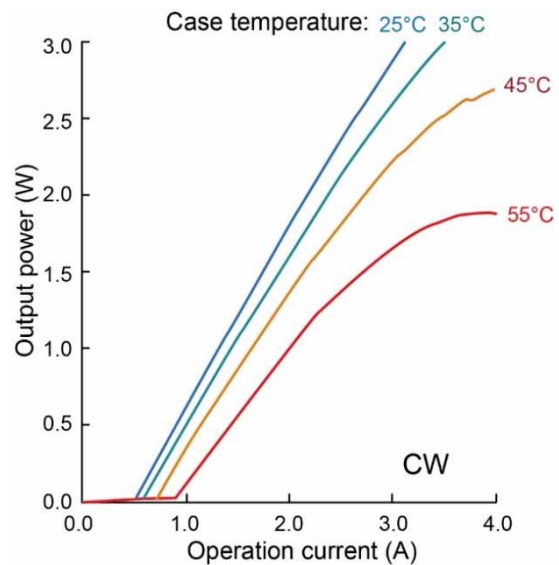


Fig. 3 Output power – Current characteristics

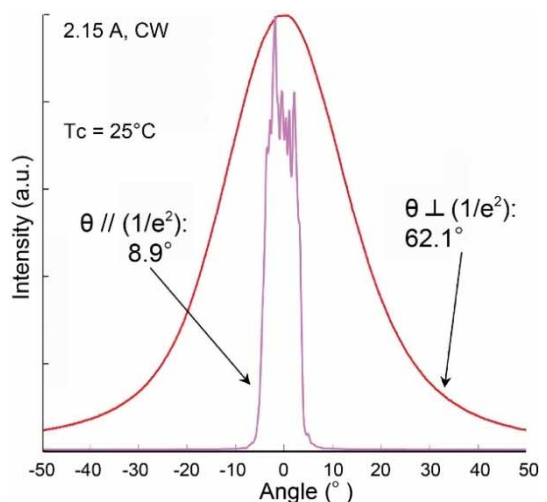


Fig. 4 FFP pattern

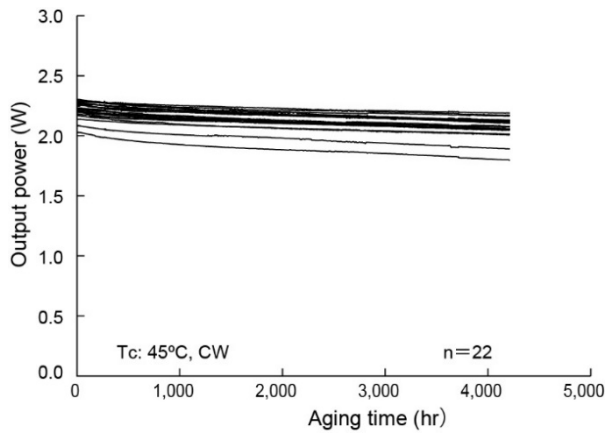


Fig. 5 Aging test results

output with constant current at the case temperature of 45°C. After 4,200 hours, the operation was stable. Under the condition of 50% reduced optical output defined as a failure, the MTTF was derived from the amount of optical output reduction in the test. As a result, the MTTF was 42,700 hours. These results show that the LD has high reliability.

The CW operation output power of 2.1 W is the world's highest output operation of a TO-CAN packaged 639-nm-band red LD.<sup>1</sup>

#### 4. Conclusion

We have placed on the market a 2.1-W output red LD that supports CW operation for projectors that require a CW light source. By optimizing the full width of the light-emitting region while using the  $\phi 9.0$ -mm TO-CAN package for existing pulse technology products, a balance was achieved between the suppression of deterioration involved in COD and favorable temperature characteristics. As a result, stability was confirmed during CW operation for 2.1-W output power for at least 23,500 hours at 45°C.

We believe that together with the pulse-operated products released previously, the new product will further improve the functionality of projectors.

# High Gain and High Power Ku-band GaN HEMT for Satellite Communication

Authors: Tetsuo Kunii\* and Hiroaki Maehara\*

In the satellite communication market, as the communication capacity and demand for mobile stations increase, the demand for higher output and smaller transmitters for satellite communication earth stations is growing. Mitsubishi Electric Corporation has developed a transmitter that operates at higher voltage and higher power density, using gallium nitride (GaN) with high dielectric breakdown voltage instead of the conventional gallium arsenide (GaAs). As part of our ongoing expansion of the lineup of amplifier devices for compact and high output transmitters, we have released a 70 W internally-matched GaN HEMT with the world's highest output (Table 1).

## 1. Characteristics of the 70 W Internally-Matched GaN HEMT

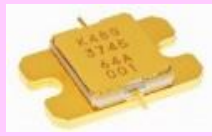
When developing the 70 W GaN HEMT, we focused on two concepts: using the same size package as the existing 50 W internally-matched GaN HEMT; and increasing the actual gain and output power compared with existing products. The purpose was to enable the amplifier output to be increased only by replacing the existing 50 W GaN HEMT used as the last stage amplifier with the 70 W GaN HEMT in a satellite communication earth station transmitter, while keeping the driver amplifier unchanged.

In order to increase the output power of a GaN HEMT, it is necessary to increase the gate width. However, increasing the gate width reduces the frequency ( $f_k$ ) required for converting the maximum stable gain (MSG) into the maximum available power

gain (MAG) due to increases in the gate resistance ( $R_g$ ) and source inductance ( $L_s$ ) per gate width, thus decreasing the gain in the desired frequency band. Given this, we considered a method to improve  $f_k$  involving reducing  $L_s$  per gate width by altering the chip layout. The transistor part of a GaN HEMT chip has a multi-finger structure in which source fingers and drain fingers are alternately arranged via gate fingers. As shown in Fig. 1(a), configuration source vias with which source electrodes are grounded are provided only on the gate side in the conventional layout. In such a configuration, an increase in the unit gate width ( $W_{gu}$ ), meaning an increase in the distance to the source vias, causes  $L_s$  to increase at the source finger edges. In the new layout shown in Fig. 1(b), the source finger edges are connected, while source vias are added to the drain side.<sup>(1)</sup> In this layout, even at the edge of each source finger,  $L_s$  per unit cell can be reduced to approximately one-half of that of the conventional products. This is the result of making the distance to the source vias shorter than in the conventional layout and increasing the number of vias per unit cell from the conventional two to four. As a result, compared with  $f_k = 14.8$  GHz at  $W_{gu} = 88 \mu\text{m}$  using the conventional layout, a good  $f_k$  value of 15.8 GHz has been achieved using the new layout even with a  $W_{gu}$  as long as 150  $\mu\text{m}$ . This indicates that a sufficient gain can be expected in the Ku band when  $W_{gu}$  is long enough to downsize a chip.

Figure 2 shows graphs of the results of evaluating the input/output characteristic of the 70 W internally-matched GaN HEMT (MGFK48G3745) for the Ku band

Table 1 Ku-band GaN MMIC and GaN HEMTs

	MGFG5H 1503 (MMIC)	MGFK47G 3745A (Internally matched HEMT)	MGFK48G 3745 (Internally matched HEMT)	MGFK49G 3745 (Internally matched HEMT)
Appearance				
Size (mm)	13.8×16.4×3.2	21.0×12.9×4.5	21.0×12.9×4.5	24.0×17.4×4.3
Output power	20 W	50 W	<b>70 W</b>	80 W
Linear gain	20 dB	8 dB	<b>10 dB</b>	7.5 dB

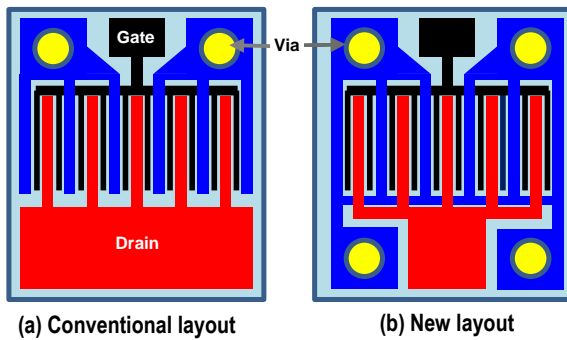


Fig. 1 Layouts of GaN HEMT Dies

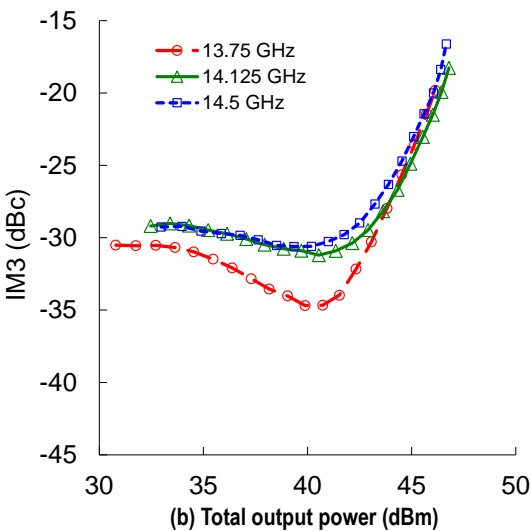
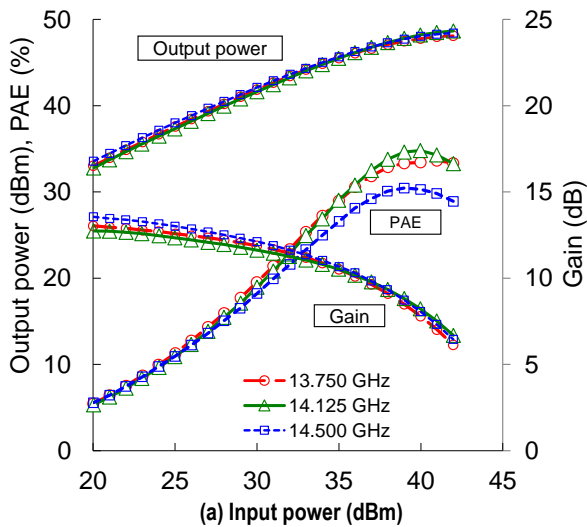


Fig. 2 RF and IM3 characteristics of Ku-band 70 W GaN HEMT (MGFK48G3745)

developed using the GaN HEMT chip described above. At a frequency of 14.125 GHz, the following favorable characteristics were obtained: saturated output power of 48.7 dBm (74.1 W), linear gain of 12 dB, and power added efficiency (PAE) of 35%. In addition, the output power (linear output power) that satisfied IM3 = -25 dBc required to secure the communication quality as a satellite communication earth station was 45 dBm. The new chip layout strikes a balance between a higher gain

and higher output, and improves the output power by approximately 40% and the linear gain by 4 dB from the existing 50 W internally-matched GaN HEMT. This compact product achieves the world's highest level of output power and linear output power.

## 2. RF Characteristics When Combined with a 20 W GaN MMIC

While GaN HEMTs are highly promising for increasing the output and reducing the size of transmitters, they often involve 'soft compression', which is a phenomenon in which the gain starts to drop at a relatively low power output compared with the power output at which the saturated output power is reached. Soft compression is a problem when GaN HEMTs are arranged in a cascade to form a multistage amplifier. The soft compression of each stage GaN HEMT superposes on one another, lowering the gain linearity of the entire amplifier from an extremely low power output, resulting in significant deterioration of the strain characteristics such as IM3. In order to solve this problem, we have released a GaN MMIC (MGFG5H1503). The GaN MMIC comes with a built-in linearizer for the driver stage to improve the strain characteristics. A test with an amplifier integrated to the existing 50 W internally matched GaN HEMT (MGFK47G3745A) verified the improvement in strain characteristics.<sup>(2)</sup> Accordingly, we have produced a multi-stage amplifier using the cascade-connected GaN MMIC with the built-in linearizer and the new 70 W internally matched HEMT (MGFK48G3745).

Figure 3 shows a schematic view of the amplifier configuration and a photo of the amplifier. The input and

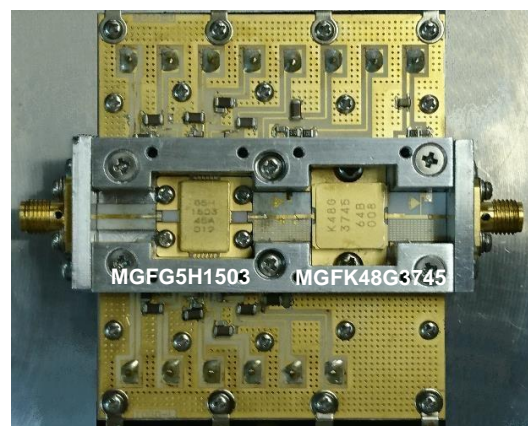
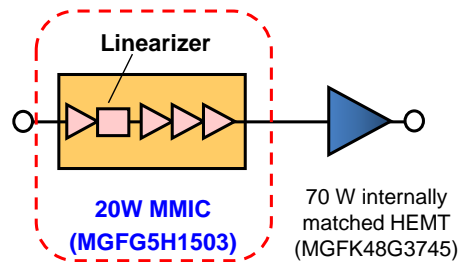


Fig. 3 Two-stage amplifier of MGFG5H1503 and MGFK48G3745 (MGFK48G3745)

output terminals and the devices are connected using  $50\ \Omega$  lines on an alumina substrate. Resin substrates with bias circuits are arranged on both sides of the alumina substrate, while an aluminum heat sink is provided on the underside of the alumina substrate to suppress the temperature increase of the GaN HEMT during operation. Figure 4 shows the results of evaluating the input/output characteristics of the amplifier. At a frequency of 14.125 GHz, the saturated output power was 48.7 dBm (74.1 W), linear gain was 37 dB, and power added efficiency was 28%. The linear output power satisfying  $IM3 = -25$  dBc was 47 dBm, an improvement of approximately 2 dB from the linear output power when a 70 W HEMT alone was operated. The use of the GaN MMIC with a built-in linearizer in the driver stage has suppressed the deterioration in strain characteristics due to soft compression, which is a disadvantage of GaN HEMT multistage amplifiers, achieving high linear output power with a GaN HEMT multistage amplifier.

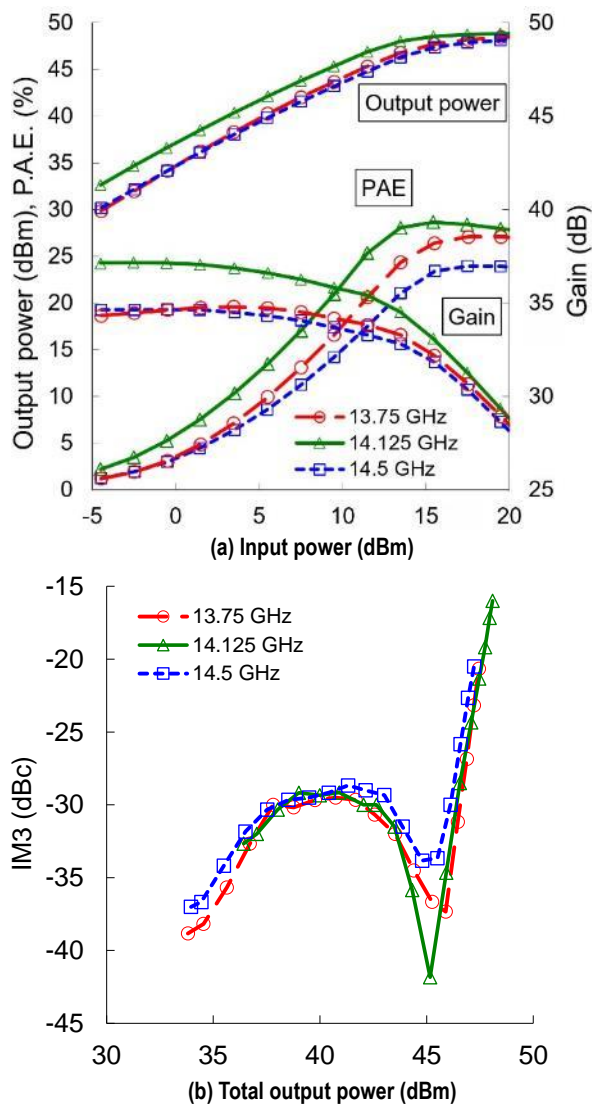


Fig. 4 RF and IM3 characteristics of 2-stage amplifier

### 3. Conclusion

We have added a 70 W internally matched GaN HEMT (MGFK48G3745) to our lineup of amplifying devices for Ku band satellite communication earth stations. The new product, with the same package size as the existing 50 W GaN HEMT, offers the world's highest level of output power. With this new product, our range of Ku band GaN devices will help increase the output power and reduce the size of transmitters for satellite communication. We will keep expanding our lineup of power amplifiers by developing devices that can operate at even higher output power and in diverse frequency bands.

The developed product uses part of our achievements in the Innovation Commercialization Venture Support Project of the New Energy and Industrial Technology Development Organization (NEDO).

### References

- (1) Imai S., et al.: A 2.6-GHz-Band 78-W Doherty Power Amplifier with GaN HEMT Unit-Cell Structure Robust for Layout-Dependent Loop Oscillation, 2016 European Microwave Conference. Dig., October (2016)
- (2) Kanaya K., et al.: A Ku-band 20 W GaN-MMIC Amplifier with Built-in Linearizer, 2014 IEEE MTT-S Int. Microwave Symp. Dig., June (2014)

# Analysis of Radiation Resistance in GaN HEMT

Authors: Takayuki Hisaka\*, Hajime Sasaki\*, Shinobu Onoda\*\* and Takeshi Ohshima\*\*

Irradiation effects of proton and Ni ions on a gallium nitride high electron mobility transistor (GaN HEMT) were investigated. The device characteristics did not degrade until  $1 \times 10^{13}$  protons/cm<sup>2</sup> for 3 MeV proton irradiation. The devices irradiated with high radiance of Ni ions had no increase in leakage current or electric field intensity, indicating there was no critical damage to the devices. These results demonstrate the device has a high radiation tolerance for space application.

## 1. Introduction

GaN HEMTs are suitable for constituting high-efficiency, high frequency, and high-power devices due to their high carrier mobility and high breakdown voltage. To obtain the advantage of high efficiency, lightweight and high reliability properties, GaN HEMTs are expected to be applied to solid-state power amplifiers (SSPAs) to be mounted on satellites<sup>(1)</sup>.

In space environments, devices mounted on satellites are exposed to space radiation consisting of high-energy electrons, protons, and heavy ions due to supernova explosions and solar activity, as well as X-rays and gamma rays generated due to the interaction of highly energetic ions with shielding. To quantify the device's tolerance to a space-specific high-radiation environment, a radiation tolerance assessment is required. Testing of the displacement damage dose (DDD) effect, single event effect (SEE), and total ionizing dose (TID) effect are the main evaluation methods of radiation tolerance.

In this study, we investigated the displacement damage produced by irradiation of protons and Ni ions on GaN HEMTs by using several optical analysis methods, ultra-high voltage electron microscopy (HVEM) and device characteristic measurements.

## 2. Ion Irradiation Test

Conventional GaN HEMTs were grown on a 4H-SiC substrate. A Schottky gate electrode was formed using sputtered TaN and Au layers<sup>(1)</sup>. 3 MeV protons and 18 MeV Ni were irradiated using an ion accelerator system<sup>(2)</sup> at the National Institutes for Quantum and Radiological Science and Technology. Protons were irradiated on the entire surface of one of the GaN HEMTs and Ni ions were irradiated in a selected area of the GaN HEMT by using a focused ion beam.

## 3. Proton Ion Irradiation Effect

Before and after proton irradiation, the DC characteristics of the devices were measured. Figure 1 shows changes in the maximum drain current ( $I_{max}$ ) with proton irradiation. At a low irradiation fluence of up to  $1 \times 10^{12}$  protons/cm<sup>2</sup>, we found a slight increase of approximately 1% in  $I_{max}$ . This increase was recoverable, because the increased  $I_{max}$  decreased to the original value after annealing at 150°C. This result means that positive charges were trapped in the devices by proton irradiation in the low fluence region. No deterioration of  $I_{max}$  was found until the irradiation fluence exceeded  $1 \times 10^{13}$  protons/cm<sup>2</sup>.

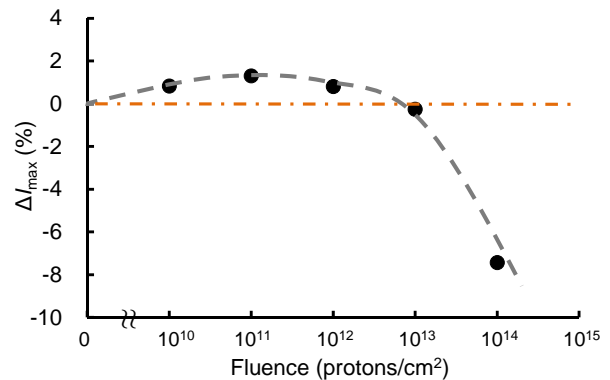


Fig. 1 Change in maximum drain current ( $I_{max}$ ) with proton irradiation

With further irradiation of  $1 \times 10^{14}$  protons/cm<sup>2</sup>,  $I_{max}$  decreased. Even in this case, critical failure such as a significant increase in gate leakage current and device breakdown did not occur. The cumulative proton irradiation amount on a satellite in geostationary orbit for 10 years is equivalent to approximately  $7 \times 10^{11}$  protons/cm<sup>2</sup> of 3 MeV protons. The influence on a device located inside the satellite is even smaller. This result indicates that GaN HEMT has sufficient resistance to protons in space environments.

## 4. Ni ion Irradiation Effect

In order to investigate the influence of displacement damage induced by ion irradiation on devices in more detail, we applied 18 MeV Ni ions as the irradiation particles.

Figure 2 shows changes in  $I_{max}$  with Ni ion irradiation.  $I_{max}$  was stable up to  $1 \times 10^{11}$  ions/cm<sup>2</sup> and started to decrease more than  $2 \times 10^{11}$  ions/cm<sup>2</sup> irradiation.

\*High Frequency & Optical Device Works

\*\*National Institutes for Quantum and Radiological Science and Technology

Compared with the proton test results in Fig. 1,  $I_{max}$  in Fig. 2 started changing at a low irradiation fluence. The result indicates that the irradiation of 18 MeV Ni ions induced larger displaced damage than 3 MeV proton irradiation.

Figure 3 shows (a) reverse and (b) forward Schottky contact characteristics of the devices before and after the Ni ion irradiation.  $I_{max}$  decreased significantly by the Ni ion irradiation at a fluence of  $5.5 \times 10^{13}$  ions/cm<sup>2</sup> as shown in Fig. 1; however, the change of gate leakage current after the irradiation is negligibly small. These results indicate that the irradiations had no significant effects on the device reliability.

In order to examine the microscopic influence of Ni ion irradiation, we applied optical measurements such as photoemission microscopy (PEM), optical beam induced resistance change (OBIRCH) imaging, and photoluminescence (PL)<sup>(3)</sup>. Electric field intensity, leakage current, and crystal quality can be observed by

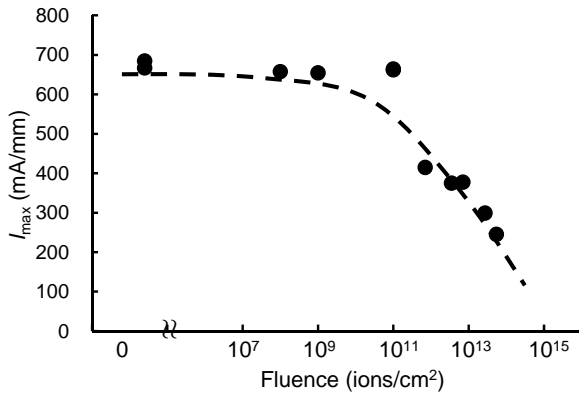


Fig. 2 Change in  $I_{max}$  with proton irradiation

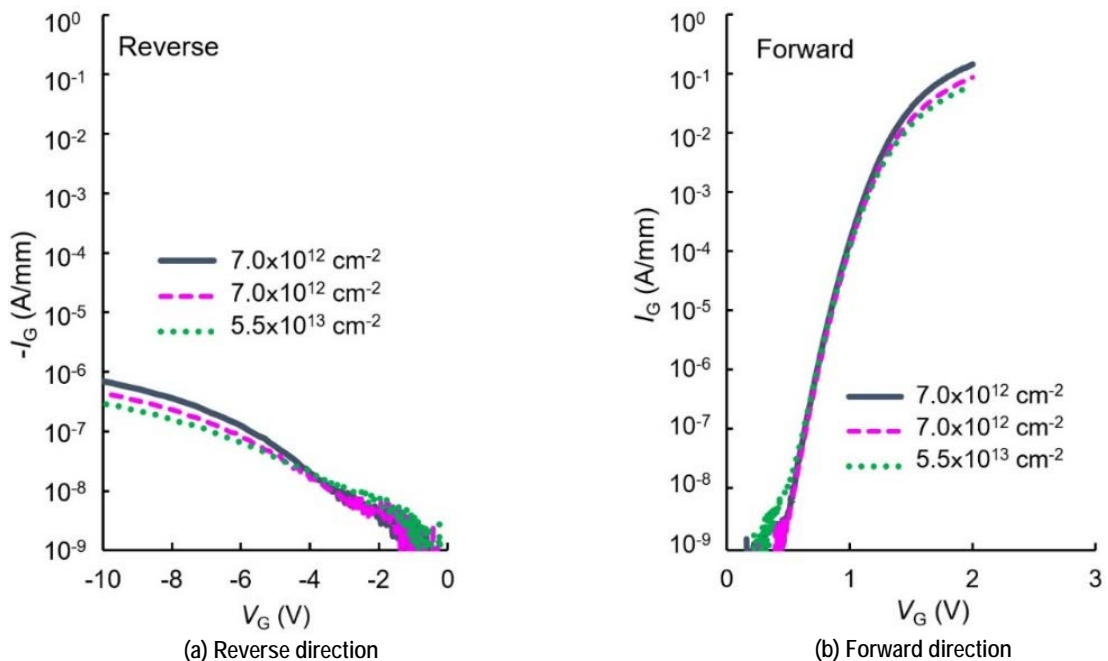


Fig. 3 (a) Reverse and (b) forward Schottky contact characteristics before and after 18 MeV Ni ion irradiation

these methods. Figure 4 shows PEM, OBIRCH, and PL images before and after Ni ion irradiation of  $7 \times 10^{12}$  ions/cm<sup>2</sup>. The irradiation area was located in the region indicated by the dotted square in Fig. 4. For the gate bias,  $-70$  V was applied during the PEM observation and  $-10$  V was applied during the OBIRCH observation. In all intensity distribution images after the Ni ion irradiation, the signal intensity uniformly decreased in the Ni-irradiated region. The decrease in each signal intensity indicates a reduction in the electric field intensity, a reduction in the leakage current and an increase in the recombination center, respectively. A spot-like signal, typically found in a device with a gate leakage current increase, cannot be found in the irradiated region. This indicates that no locally concentrated electric field or gate leakage was caused by the irradiation. This is consistent with the fact that no increase in the gate leakage current was observed in Fig. 3. Therefore, the results described above suggest that the Ni ion irradiation caused a uniform reduction in the carrier concentration, preventing a concentrated electric field that would lead to a significant increase in the gate leakage current.

We investigated the influence of ion irradiation on the GaN HEMT microscopically. When a semiconductor device is irradiated with high-energy ions, irradiation damage occurs due to the displacement of crystal atoms from regular lattice positions. Figure 5 shows a cross-sectional transmission electron microscopy (TEM) image taken after irradiation; for the observation, we irradiated the GaN HEMT with  $2.8 \times 10^{13}$  ions/cm<sup>2</sup> of Ni ions at 18 MeV. A sample thickness of  $1.5 \mu\text{m}$  was observed by

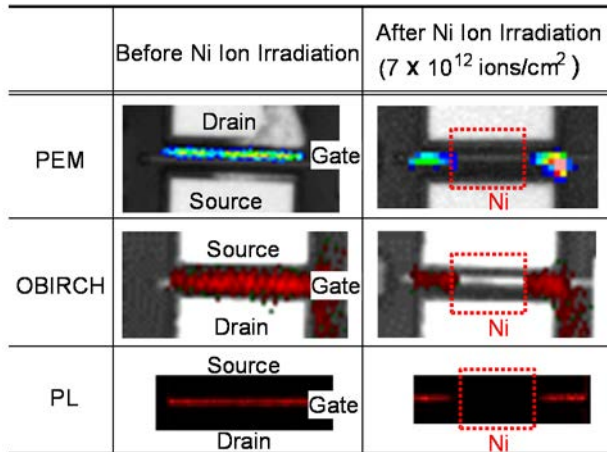


Fig. 4 PEM, OBIRCH and PL images before and after Ni ion irradiation

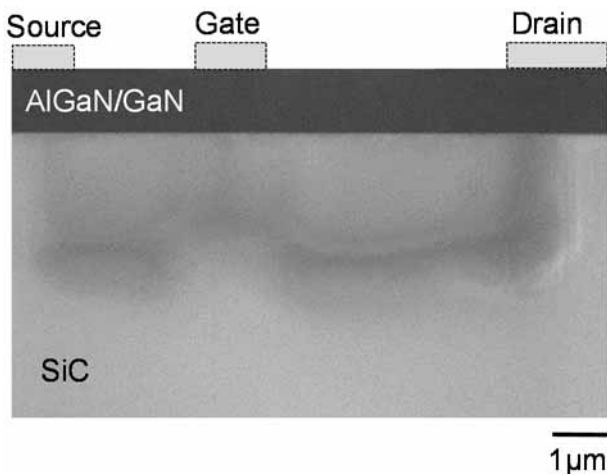


Fig. 5 Cross-sectional TEM image of the AlGaIn/GaN HEMT after Ni ion irradiation

an acceleration voltage of 2 MV using an ultra-high voltage electron microscope (H-3000)<sup>(6)</sup>. A darker shape was observed in the SiC substrate region below the AlGaIn/GaN layer, corresponding to the irradiation damage. The damage reached a depth of approximately 4 μm in the SiC substrate. The damage was also found under the gate electrode, although the damage slightly shifted to the gate electrode. The shift indicates that the energy of Ni ions is decreased by the gate electrode.

The lattice defects were supposed to be created near the AlGaIn/GaN channel layer, causing a decrease in the carrier concentration and mobility. This is likely to have caused a decrease in the drain current. Figure 5 shows no line-type defects caused along the ion track. It is consistent with the results of no increase in gate leakage current and electric field concentration.

## 5. Conclusion

Irradiation experiments of ions to GaN HEMTs indicate that the device would be stable up to a fluence of  $1 \times 10^{13}$  protons/cm<sup>2</sup> for 3 MeV proton and  $1 \times 10^{11}$  ions/cm<sup>2</sup> for 18 MeV Ni ions. Excessive ion irradiation caused a decrease in the drain current, but did not cause a concentrated electric field or an increase in the gate leakage current. GaN HEMTs had sufficient radiation tolerance in space environments.

## References

- (1) Yamasaki, T., et al.: A 68% Efficiency, C-Band 100W GaN Power Amplifier for Space Applications, Proc. Microwave Symp. Dig. MTT-S Int., 1384–1387 (2010).
- (2) Onoda, S., et al.: Enhanced Charge Collection by Single Ion Strike in AlGaIn/GaN HEMTs, IEEE Trans. On Nuclear Science, 60(6), 4446–4450 (2013).
- (3) Sasaki, H., et al.: Irradiation Effect of Ions on AlGaIn/GaN HEMTs, ROCS Workshop Proceedings, 59–67 (2016).
- (4) Ziegler, J.F., et al.: The Stopping and Range of Ions in Solids, Vol. 1, New York: Pergamon Press (1985).
- (5) Advanced Characterization Nanotechnology Platform, Research Center for Ultra-High Voltage Electron Microscopy, Osaka University, <http://www.uhvem.osaka-u.ac.jp/nanoplatform-kouzoukaiseki/index.html>.

